processes

MDPI

Article

Computational Fluid Dynamics and Population Balance Model Enhances the Smart Manufacturing and Performance Optimization of an Innovative Precipitation Reactor

Antonello Raponi [1,*,†], Diego Fida [1], Fabrizio Vicari [2], Andrea Cipollina [3] and Daniele Marchisio [1]

[1] Department of Applied Science and Technology, Institute of Chemical Engineering, Politecnico di Torino, 10129 Torino, Italy; diego.fida@polito.it (D.F.); daniele.marchisio@polito.it (D.M.)
[2] ResourSEAs srl, 90141 Palermo, Italy; fabrizio.vicari@resourseas.com
[3] Dipartimento di Ingegneria, Università degli Studi di Palermo—Viale delle Scienze Ed.6, 90128 Palermo, Italy; andrea.cipollina@unipa.it
* Correspondence: antonello.raponi@polito.it
† Current address: Davidson School of Chemical Engineering, Purdue University, West Lafayette, IN 47907, USA.

Abstract: In this study, we propose the study of an innovative precipitation prototype designed by ResourSEAs, guided by a CFD-PBM (Computational Fluid Dynamics and Population Balance Model) approach, aiming to understand the influence of reactant concentration and nozzle orientation on precipitation processes. The first part of the study examines the effect of reactant concentration on supersaturation and the zeroth-order moment (m_0) within a controlled flow and turbulence fields. Three different concentrations of Mg^{2+} (0.1, 0.3, and 0.6 M) and OH^- (0.005, 0.01, and 0.02 M) were tested, resulting in varying supersaturation profiles and m_0 fields. Our results show that, under equal turbulence conditions, increasing the concentration of reactants beyond a certain point actually slows down mixing, which in turn hinders the generation of supersaturation. As a result, supersaturation profiles become nearly identical to those of lower concentrations, despite having consumed more reactants. The second part of this study focuses on the effect of nozzle orientation and positioning along the prototype axis on reactant mixing and particle formation. The simulations reveal that nozzle orientation has a significant impact on the formation of primary particles, especially when positioned in low-velocity regions, leading to slower mixing and greater particle growth. Conversely, high-velocity regions promote faster mixing and more intense aggregation. These findings highlight the interplay between concentration, nozzle orientation, and flow conditions in determining precipitation efficiency, offering insights for optimizing reactor design in industrial applications.

Keywords: population balance modelling; smart manufacturing; digital twins; computational fluid dynamics; magnesium hydroxide precipitation

Academic Editor: Krzysztof Rogowski

Received: 11 April 2025
Revised: 5 May 2025
Accepted: 14 May 2025
Published: 31 May 2025

Citation: Raponi, A.; Fida, D.; Vicari, F.; Cipollina, A.; Marchisio, D. Computational Fluid Dynamics and Population Balance Model Enhances the Smart Manufacturing and Performance Optimization of an Innovative Precipitation Reactor. *Processes* **2025**, *13*, 1721. https://doi.org/10.3390/pr13061721

1. Introduction

In recent years, Mg has been included in the critical raw materials list. As a consequence, the number of studies on how to recover it from non-conventional sources, such as waste brines or bitterns, has increased. In this regard, the synthesis of $Mg(OH)_2$ is one of the most widely used means of recovery, due the multitude of applications in which $Mg(OH)_2$ can be employed [1–7].

The first recovery route was the hydrothermal process [8], which was replaced due to its high energy demand. Therefore, less energetic alternatives have attracted attention [9]. One of them is the precipitation [10] of $Mg(OH)_2$ from brines or bitterns as a

result of the reaction between the Mg^{2+} and an alkaline solution (e.g., NaOH). The reaction produces increasing supersaturation levels that, in turn, directly trigger primary (or molecular) processes, such as primary nucleation and molecular growth. The occurrence of primary processes leads to the formation of 'primary particles'. In addition to the molecular processes, secondary processes can occur, as follows: (i) agglomeration (weak physical interaction between primary particles due to the presence of liquid) and (ii) aggregation (strong chemical interaction resulting in the formation of a crystalline bridge between primary particles) [11].

The presence of processes occurring at the molecular scale (i.e., primary nucleation and growth), at the meso-scale (i.e., agglomeration and aggregation), and at the macro-scale (i.e., fluid motion) make precipitation a complex process whose modelling needs to account for this multi-scale nature. Due to the fast rates, one of the key aspects to account for in precipitation is mixing at all scales [12–14]. In fact, the combination of macro- and micro-mixing determines how fast (or slowly) the reactant reach the molecular scale (i.e., the Batchelor scale) and react influencing all the precipitation phenomena downstream. Although in some cases the mixing modelling in precipitation can be neglected [15], in the majority of cases it is essential to include it. Danckwerts [16], Becker and Larson [17] were among the first to introduce the micro-mixing effect in fast reactions. In recent years, with the increase in computing power, many researchers have studied the influence of mixing on various processes by resorting to Computational Fluid Dynamics (CFD) simulations and experimental validation [18]. Schikarski et al. [19,20] proposed a detailed numerical assessment and experimental validation of the mixing in static mixers, employing Direct Numerical Simulations (DNS). On the other hand, less computationally expensive approaches can be used. Shiea et al. [21] proposed a Reynolds-Averaged Navier–Stokes equation (RANS) approach and a multi-environment model to integrate the micro-mixing effect in the co-precipitation modelling of Ni-Mn-Co hydroxide. Analogously, in previous publications of ours, we introduced a Population Balance Model (PBM) coupled with CFD simulations in the RANS framework to model $Mg(OH)_2$ precipitation. We built the model [22], tuned it by identifying its parameters [23] using a novel machine learning methodology, and validated it [24].

In this contribution, we use the same validated model to assess the effect of variation in design parameters within the possible range covered by the producer of the prototype by investigating the influence of turbulence and, consequently, mixing on the precipitation process. In Section 2, the prototype is presented and Large Eddy Simulations (LES) are exploited to characterize and validate the flow field due to the lack of experimental data corresponding to the study. In Section 3, we introduce the CFD-PBM model, emphasizing the relationship between turbulence, mixing, and precipitation phenomena. To conclude, in Section 4, we present two cases. The first assesses the influence of the reactant concentration at constant flow rates on precipitation, while the second assesses the influence of turbulence and, therefore, mixing on the precipitation process as a function of the feeding zone. Lastly, in Section 6, we draw relevant conclusions.

2. Materials and Methods

In recent years, a collaborative effort between ResourSEAs srl and the University of Palermo led to the development and construction of a pilot-scale prototype for $Mg(OH)_2$ precipitation to recover Mg^{2+} from various kinds of brines [25]. This system has since been patented by ResourSEAs srl [26]. However, at first, the design process was led by trial and error rather than following any guidelines suggested by a numerical framework. This work aims to bridge this gap, demonstrating the practical value of modelling approaches in the context of smart manufacturing. In this work, we go through an analysis of the design

parameters, exploring the ranges covered by the patent, to optimize the performance of the prototype. The prototype features a tubular design with several inlet streams and can be mathematically described as a Multi-Feed Plug Flow Reactor (MF-PFR). A schematic illustration of the MF-PFR is shown in Figure 1.

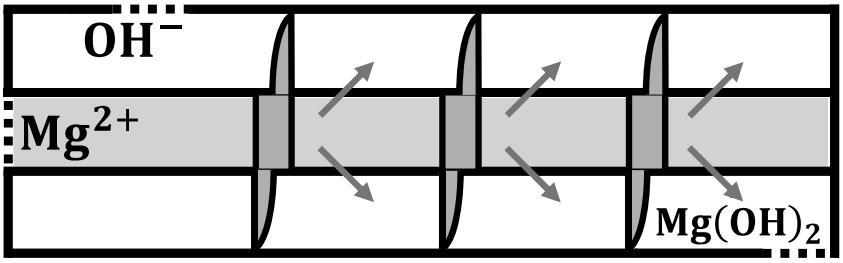

Figure 1. MF-PFR schematic representation.

The prototype consists of an inner and outer tube, and the two environments exchange transport properties thanks to the presence of nozzles. Along the reactor, there are propellers whose purpose is to create a rotational motion to promote the mixing of reactants. $MgCl_2$ is fed into the inner tube, and NaOH into the outer crown. The reactants, therefore, react in the outer crown according to the following reaction:

$$Mg^{2+}{}_{(aq)} + 2OH^{-}{}_{(aq)} \rightarrow Mg(OH)_{2(s)} \downarrow \quad (1)$$

To preserve confidentiality, all parameters subject to patent protection are expressed in a dimensionless form. However, the analysis that guided the design and performance optimization is provided in full. Given the periodic nature of the device, where identical mixing conditions repeat between consecutive propellers, our study focuses on the precipitation process that occurs between two propellers. This approach allows us to isolate and investigate the impact of local mixing conditions on the precipitation process while maintaining the representativeness of the overall behavior of the prototype. For the sake of clarity, the wireframe of the geometry is presented in Figure 2.

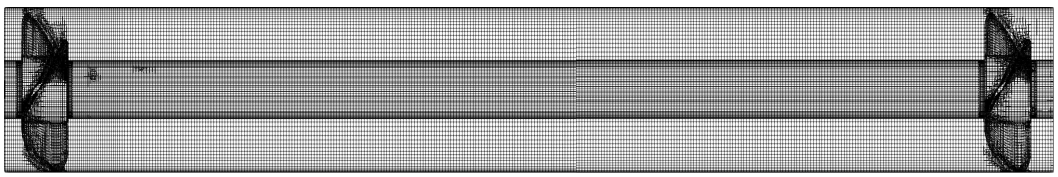

Figure 2. Geometry wireframe.

The geometry presented in Figure 2 is our template. This means that, depending on the operating conditions, we changed the length of the tubes, the number of nozzles, and their position and/or orientation, but we kept the propeller type, its orientation, and the tube diameters constant. Further details on the mesh and grid convergence are reported in the 'Supplementary Materials'.

Flow Field and Turbulence Model and Simulation Setup

The formation of low-solubility compounds is strongly influenced by mixing behavior, and thus by the fluid flow characteristics of the system. At high *Re* numbers, the choice of turbulence model can substantially impact the predicted flow patterns and, consequently, the precipitation outcomes [15,24]. In the absence of experimental data, Large Eddies Simulations (LES) offer higher accuracy compared to Reynolds-Averaged Navier–Stoke (RANS) models, but are much more time-consuming. Therefore, the LES were used to select the RANS model that was best able to mimic the LES steady-state solution. In LES, the

large-scale turbulent structures (eddies), which carry most of the turbulent kinetic energy, are solved explicitly, whereas the smaller subgrid-scale (SGS) eddies are modeled. The LES methodology is based on the filtered Navier–Stokes equations, which separate the velocity field, u, into a resolved component, $\bar{u}$, and a subgrid-scale component, u'. Therefore, by substituting the decomposed velocity and employing the Boussinesq hypothesis, the Navier–Stokes equations, for an incompressible Newtonian fluid, become the following:

$$\frac{\partial \mathbf{u}^{(GS)}}{\partial t} + \mathbf{u}^{(GS)} \cdot \nabla \mathbf{u}^{(GS)} = -\frac{1}{\rho}\nabla p^{(GS)} + (\nu + \nu_t)\nabla^2 \mathbf{u}^{(GS)} + \mathbf{g} \quad (2)$$

where $\bar{p}$ is the pressure field, ρ is the fluid density, ν is the kinematic viscosity and $\mathbf{g}$ is the gravitational acceleration. ν_t is the turbulent kinematic viscosity and it is approximated using a turbulence model. The RANS approach, on the other hand, relies on time-averaging the Navier–Stokes equations, decomposing the velocity field into mean and fluctuating components. Unlike LES, where only the smallest scales are modelled, RANS models approximate the entire turbulence spectrum, making them computationally cheaper but potentially less accurate. In this contribution, the RANS model candidates include the standard $k-\varepsilon$, $k-\varepsilon$ RNG, and $k-\omega$ SST. The LES candidate, instead, is the k-equation (kEq) model, a one-equation LES model. In Table 1, we report the boundary conditions (BC).

Table 1. Boundary conditions used for the simulations.

Boundary	Velocity	Pressure	Turbulence Fields
Inlet	Flowrate	Neumann	Correlation
Outlet	Neumann	0	Neumann
Inner tube	No-slip	Neumann	Wall function
Outer tube	No-slip	Neumann	Wall function
Propeller (stationary)	No-slip	Neumann	Wall function
Nozzles	Flowrate	Neumann	Correlation

To enhance the stability and accelerate the convergence of the LES simulations, these were initialized using the solution derived from the standard $k-\varepsilon$ turbulence model. Each LES run continued for a duration corresponding to 10 residence times, which was sufficient to obtain results statistically independent of the initial conditions [27]. To confirm this independence, an additional LES was initialized using the $k-\omega$ SST model, yielding equivalent results. This validated the assumption that 10 residence times are adequate to eliminate sensitivity to initial conditions. The computational mesh was designed to capture at least 80% of the turbulent kinetic energy [28]. Accordingly, the characteristic grid size was determined by calculating the maximum allowable cell dimension using Equation (3):

$$\max(\Delta) = \frac{1}{5}\min(l_0) \quad (3)$$

l_0 was obtained from the RANS simulation and corresponds to the integral length scale, defined as follows:

$$l_0 = \left(\frac{k^{3/2}}{\varepsilon}\right)^{1/4} = \frac{k^{\frac{1}{2}}}{\omega\, C_\mu^{\frac{1}{4}}} \quad (4)$$

Equation (3), therefore, establishes that the maximum value for the SGS in the LES should not exceed 20% (i.e., 1/5) of the minimum among the largest eddy size (l_0) in the system.

Figure 3 highlights the significant influence of the vortex formed downstream of the blade. This structure corresponds to a fluid region characterized by high residence times. A comparison of the vortex dimensions clearly reveals that the standard $k-\varepsilon$

model (Figure 3a) yields results that markedly deviate from those obtained with the other turbulence models. In the case of the standard $k-\varepsilon$ model, the vortex does not extend far beyond the propeller, whereas all the others develop a vortex with a dimensionless axial coordinate of 0.2. A quantitative assessment was also performed by calculating, for each cell, the error in the turbulent kinetic energy. For RANS, the turbulent kinetic energy field (k_{RANS}) was directly available through obtaining the solution of the transport equation for k. For LES, the turbulent kinetic energy field (k_{LES}) was reconstructed as the sum of the modelled contribution, $k^{(SGS)}$, and the resolved contribution, $k^{(GS)}$. The former was immediately available from the LES simulation, whereas the latter was calculated as follows:

$$k^{(GS)} = \frac{1}{2}\sum_i u_i' u_i' \tag{5}$$

where u' is the fluctuating velocity. This was calculated as the difference between the resolved velocity and its time average. The error for the i-th cell, therefore, was defined as follows:

$$\varphi_{\mathrm{err},i} = \frac{|k_{\mathrm{RANS},i} - k_{\mathrm{LES},i}|}{\max(k_{\mathrm{RANS},i}, k_{\mathrm{LES},i})} \tag{6}$$

Through construction, this will tend toward 0 if the RANS and LES values overlap in the i-th cell and toward 1 if their values deviate. The distribution function of the error was defined as follows:

$$f_i(\varphi) = \frac{\sum_j V_j}{V_{tot}} \frac{1}{\varphi_{\mathrm{err},i+1} - \varphi_{\mathrm{err},i}} \tag{7}$$

$$\sum_i [f_i(\varphi)(\varphi_{i+1} - \varphi_i)] = 1 \tag{8}$$

Equation (7) represents the volume fraction of the system, whose error is between $\varphi_{\mathrm{err},i}$ and $\varphi_{\mathrm{err},i+1}$.

Figure 4 presents a comparison of the error distribution functions for the three RANS models and the k-Eq model. The results indicate a notable deviation for the k when using the standard $k-\varepsilon$ model. The distribution function shows higher values in bins closer to 1, leading to an average error that is nearly four orders of magnitude larger than those obtained with the k-Eq model. Both the $k-\varepsilon$ RNG and $k-\omega$ SST models exhibit large regions where the turbulent kinetic energy values are in close agreement with those obtained from the LES simulations. Furthermore, while the difference is relatively small, it is worth noting that the $k-\varepsilon$ RNG and $k-\omega$ SST models also show some discrepancies compared to LES, particularly in the reactor region before the propellers, an area that is not directly impacted by the reactants. This discrepancy can be attributed to the absence of vortex formation before the blades, resulting in a solution with a lower-intensity turbulence and fewer explicitly resolved features. As a consequence, the standard $k-\varepsilon$ model produces results that significantly differ from those of the other models, which are more consistent with one another. A comparison was performed between the $k-\varepsilon$ RNG and $k-\omega$ SST models using an analogous error metric defined as follows:

$$\varphi_{\mathrm{err}_2,i} = \frac{|k_{k-\varepsilon\ \mathrm{RNG},i} - k_{k-\omega\ \mathrm{SST},i}|}{max(k_{k-\varepsilon\ \mathrm{RNG}}, k_{k-\omega\ \mathrm{SST}})} \tag{9}$$

Here, $k_{k-\varepsilon\ RNG}$ and $k_{k-\omega\ SST}$ represent the turbulent kinetic energy values returned from the $k-\varepsilon$ RNG and $k-\omega$ SST models, respectively. The distribution function is shown in Figure 5.

The turbulence models predict comparable results, with an average error of 0.3. In conclusion, the standard $k-\varepsilon$ model was excluded for the reasons discussed earlier, and

the $k-\omega$ SST model was selected. Similar to the $k-\omega$ SST model, the $k-\varepsilon$ RNG also produces results in line with the LES simulations. However, the $k-\omega$ SST model was preferred over the $k-\varepsilon$ RNG due to its lower computational cost.

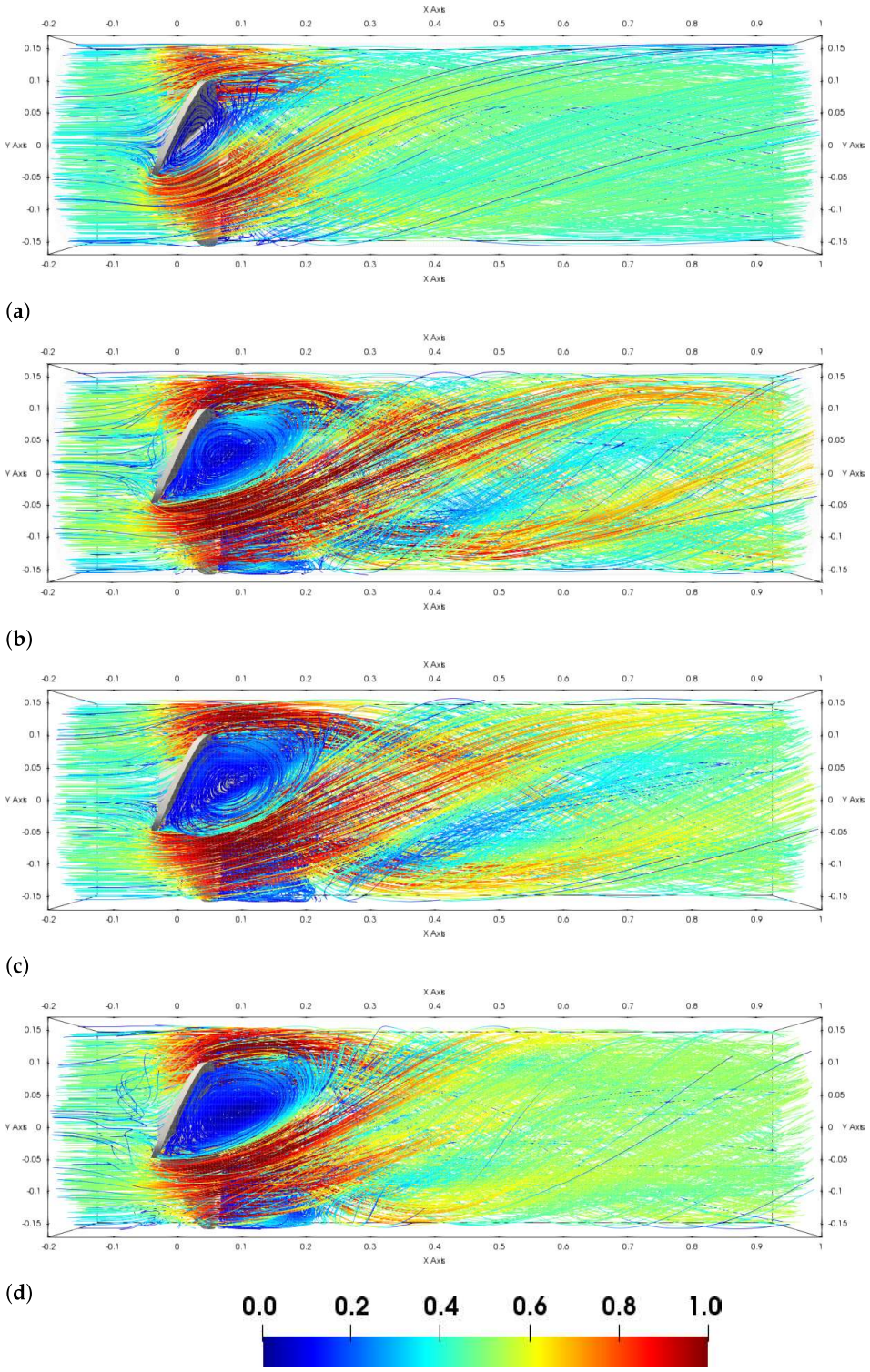

Figure 3. Velocity field displayed on streamlines for (**a**) standard $k-\varepsilon$; (**b**) $k-\varepsilon$ RNG; (**c**) $k-\omega$ SST; and (**d**) k-Eq.